RSC Advances

PAPER

View Article Online
View Journal | View Issue

Check for updates

Cite this: *RSC Adv.*, 2019, **9**, 10305

Fe(II) and Mn(II) removal by Ca(II)–manganite (γ-MnOOH)-modified red mud granules in water

Yingying Su,[a] Qi Zhu, *[a] Jian Li,[a] Dongdong Wang,[a] Zipeng Xing*[a] and Lei Fang*[b]

Received 7th January 2019
Accepted 18th March 2019

DOI: 10.1039/c9ra00123a

rsc.li/rsc-advances

In this study, a material (DLRMG) was synthesized by modifying Ca^{2+} and manganite (γ-MnOOH) on red mud granules (RMG), which were the main raw materials derived from industrial alumina. Moreover, a series of experiments were conducted on the adsorption of Fe^{2+} and Mn^{2+} in underground water. The prepared samples were analyzed by X-ray diffraction (XRD), thermogravimetric analysis-differential thermal analysis (TG-DTA), zeta potential analysis, BET and scanning electron microscopy (SEM); the concentration of the effluent was found to be of acceptable standard after the treatment. DLRMG continued to treat fluoride wastewater even after the saturated adsorption of Fe^{2+} and Mn^{2+}, and the results clearly showed that the treatment was effective. Overall, the problems of red mud stockpile and pollution in China would be effectively controlled by DLRMG.

1. Introduction

Groundwater is a major source of water for industrial use, agricultural production and residents in China; it usually has adequate quality as it is filtered and adsorbed by the strata and not readily affected by human activities; however, due to the overall improvement of industry and agriculture, the pollution of groundwater is becoming a significantly serious concern. In this regard, an effective treatment of groundwater has drawn significant attention.[1,2] Groundwater is generally hypoxic and weakly alkaline under natural conditions. The regional groundwater that flows through the minerals, rocks and other substances often contains elements, such as Fe^{2+} and Mn^{2+}, owing to the physical and chemical reactions; moreover, some metal ions enter groundwater *via* various ways due to the continuous flow of groundwater, and this leads to an increase in the concentration of metal ions in groundwater beyond the safety standards. In addition, the industrial and agricultural pollution can exacerbate groundwater pollution.

The major source of drinking water in rural areas is groundwater, and the existing status of Fe^{2+} and Mn^{2+} in groundwater exceeds the safety standards in some areas;[3,4] according to the drinking water health standards of China (GB54789-2006), the Fe^{2+} content in drinking water should not be more than 0.3 mg L^{-1} and the Mn^{2+} content in drinking water should not be more than 0.1 mg L^{-1} because water containing Fe^{2+} and Mn^{2+} in excess is harmful for drinking in the long run. An excessive intake of Fe^{2+} and Mn^{2+} can result in osteoporosis, liver cirrhosis, Parkinson's disease and damage to the central nervous system of humans, leading to organ damage;[5–7] in addition, excess Fe^{2+} and Mn^{2+} in water can lead to mass problems in some aspects of industrial production. In industrial production, groundwater containing Fe^{2+} and Mn^{2+} should not be used as boiler water. Fe^{2+} and Mn^{2+} will form scales, which will affect the energy transfer, reduce the production efficiency, and even block the cooling pipe. In the textile industry, the use of untreated water containing Fe^{2+} and Mn^{2+} leads to the fixation of these ions to the fiber; this leaves rust on the fabric; during dyeing operations, Fe^{2+} and Mn^{2+} can bind to dyes and affect the dyeing process; in bleaching, Fe^{2+} and Mn^{2+} catalyze the decomposition of bleach; this makes bleaching difficult. During papermaking, the pulp turns yellow because of the adsorption of Fe^{2+} and Mn^{2+} between cellulose.[8] Both Fe^{2+} and Mn^{2+} are transition elements and have the same valence electron configuration; therefore, Fe^{2+} and Mn^{2+} always co-exist in groundwater;[9] the conventional methods for Fe^{2+} and Mn^{2+} processing include oxidation (biological oxidation, contact oxidation, and chemical oxidation), ion exchange, adsorption and so on;[10–14] moreover, different treatment measures can be applied to treat various wastewaters; among these methods, adsorption is commonly used because of its simple operation, better removal effect, ease in recovery after adsorption and no secondary pollution. The selection of a proper adsorbent is crucial in the removal of heavy metals by adsorption; therefore, the selection of an excellent adsorbent has become a hot topic of research in the scientific community. At present, the main adsorbents used are activated carbon, zeolite, fly ash and so on.[15–17]

Red mud produced by the alumina industry generates significant waste.[18,19] Red mud is easily available and can function as an efficient filtration material through a simple treatment. Numerous

---

[a] School of Chemistry and Materials Science, Key Laboratory of Chemical Engineering Process & Technology for High-efficiency Conversion, Heilongjiang University, China. E-mail: hdzhuqi@126.com; xzphit@126.com; cherry1999_0@163.com

[b] School of Food Engineering, Harbin University, Harbin 150080, China

studies have shown that red mud has a good treatment effect on the adsorption of heavy metals (*e.g.*, arsenic, lead, and cadmium), various salts (*e.g.*, sulfate and nitrate) and organic pollutants due to its sustainable use, porous surface structure, and easy separation from muddy water;[20–22] this solves the problem of disposal of excessive red mud, and the resource utilization of waste can be achieved; therefore, the use of pulverized coal and bentonite-prepared red mud ball for the filtration of drinking water has significant benefits. In previous studies, red mud has been used as a functional filter material to remove pollutants from water.[23] Based on the abovementioned facts, herein, the synthesis of a new material *via* impregnation of Ca^{2+} and γ-MnOOH on RMG was carried out, and the resultant material could effectively remove excess Fe^{2+} and Mn^{2+} from water; moreover, the RMG filter material could be recycled and retreated; herein, the Fe^{2+} and Mn^{2+} contents of the water sample were adjusted according to those in the underground drinking water in small towns to simulate the actual groundwater conditions.[24,25] A series of batch experiments for the optimization of several parameters, including adsorption time, solution pH and adsorbent addition dosage, were designed. The surface properties of the DLRMG and the mechanism of Fe^{2+} and Mn^{2+} removal have been discussed using various testing methods. The impregnation of Ca^{2+} and γ-MnOOH onto RMG is a new research topic, which has not been reported to date. In addition, it was of vital importance to retreat the filter material after saturation adsorption. There was also a small amount of excess F^- in groundwater, and excessive intake of F^- could cause a series of adverse effects on people such as on teeth and bones;[26] finally, to achieve recycling of the filter media, saturated adsorptions of Fe^{2+} and Mn^{2+} filter media were conducted during the treatment of F^- in water.

2. Material and methods

2.1 Chemicals and materials

The red mud raw materials used in this experiment were obtained from China Shandong Aluminum Industry Company. Polyvinyl alcohol (PVA), bentonite, hydrochloric acid, acetic acid, concentrated sulfuric acid, polyethylene glycol-400, hydroxylamine hydrochloride, 1,10-phenanthroline monohydrate, potassium, pyrophosphate, potassium periodate, ammonia water, sodium salt, potassium permanganate, sodium hydrogen sulfite, sodium fluoride, sodium nitrate, and calcium chloride were obtained from Tianjin Kermel Reagent Co. and were of analytical grade; all the solutions in the experiments were prepared using deionized water.

2.2 Characterization methods

The composition of red mud was investigated using X-ray fluorescence analysis (PANalytical, AXIOS-PW4400, The Netherlands), and the results are shown in Table 1. The X-ray diffraction (XRD) patterns of the samples were obtained using the Rigaku D/max-IIIB X-ray diffractometer with Cu Kα radiation ($\lambda = 1.5406$ Å) generated at 40 kV and 20 mA. The Brunauer–Emmett–Teller (BET) surface areas of the samples were determined using the N_2 adsorption isotherms obtained *via* the Micromeritics ASAP 2420 instrument, and the plot of the pore-diameter distribution was determined using the Barrett–Joyner–Halenda (BJH) method from the desorption branch of the isotherm. Micromorphological characteristics of the samples were characterized using the Hitachi S-4800 scanning electron microscope (SEM) with an accelerating voltage of 5.0 kV. The TG/DTA analysis was conducted using the Setaram-Labsys thermal analyzer. The surface charges of the supported sample were determined using a zeta-potential analyzer (Horiba, SZ-100Z, France). The amount of Fe was determined using a phenanthroline spectrophotometric method. The manganese ion content was measured using potassium periodate spectrophotometry. Fluorine was measured using an ion selective electrode method.

2.3 Sample preparation

2.3.1 Preparation of the RMG filter material. The RMG raw powder material is a mixture of red mud, bentonite, and pulverized coal. All the raw materials were screened and then ball milled at the mixing ratio of 90 : 4 : 6. A certain amount of the abovementioned mixture powder and polyvinyl alcohol were mixed and stirred at 70 °C until they were muddy and attained a shape like a sieve ball, which was about 1 mm in size.[27] After drying, the spherical particles were placed in a muffle furnace, calcined at 1030 °C and then acquired.

2.3.2 Preparation of the γ-MnOOH/RMG (SLRMG) filter material. Herein, to 0.1360 g of potassium permanganate dissolved in 50 mL of deionized water, PEG-400 was added followed by stirring for 1 h; then, the solution was transferred to a 100 mL stainless steel reactor.[28] The reaction was carried out at 120 °C for 12 hours, and then, the reaction mixture was naturally cooled down to room temperature; after being cooled down, the obtained filter material was rinsed repeatedly with deionized water and ethanol till neutral and then dried for use. During the reaction in the stainless steel reactor, the same procedure was repeated to prepare γ-MnOOH by adding 1 g of RMG. Thus, we obtained a single loaded RMG (SLRMG) material.

2.3.3 Preparation of the Ca^{2+}–manganite/RMG (DLRMG) filter material. Typically, 1 g of SLRMG was added to a 10 mL (0.5 mg L^{-1}) calcium chloride solution; the solution was then placed in a water bath at 90 °C for four hours after being shaken for 1 h. The obtained filter material was washed repeatedly with clear water, then dried and stored. Finally, the double-loaded RMG (DLRMG) material was obtained for use.

Table 1 The composition of red mud (wt%)

Composition	SiO_2	Fe_2O_3	Al_2O_3	Na_2O	TiO_2	CaO	SO_3	K_2O	P_2O_5
Red mud	36.338	28.030	22.846	8.864	1.781	1.078	0.399	0.121	0.168

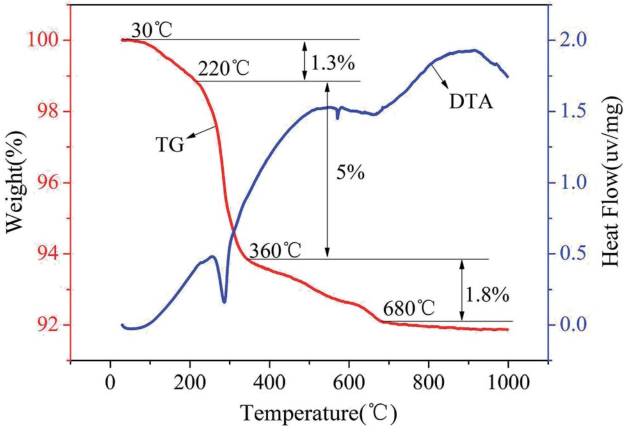

Fig. 1 TG/DTA curves of the ceramic filter material.

2.3.4 Experiments of Fe^{2+} and Mn^{2+} removal. A series of batch experiments were carried out based on the ability of RMG to remove Fe^{2+} and Mn^{2+} before and after loading Ca^{2+} and γ-MnOOH. Briefly, 0.15 g of RMG and DLRMG material were mixed in a 100 mL beaker, which contained 20 mL of (2 mg L^{-1} and 1 mg L^{-1}) Fe^{2+} and Mn^{2+} solution at pH 7. The experiment was performed at 120 rpm at room temperature; the supernatant obtained after shaking was filtered using 0.45 filters, and then, the concentration was measured using a spectrophotometer. The blank experiment and parallel experiment were set up, and each experiment was repeated thrice.

3. Results and discussion

3.1 Characterization of the sample

3.1.1 Preliminary selection of the sintering temperature. Thermogravimetric analysis was performed on the mixed raw materials, and the TG-DTA curve is shown in Fig. 1. With a continuous increase in temperature, the filter element exhibits different degrees of weight loss, and it may be mainly divided into two stages; the first stage of weight loss is from 30 °C to 220 °C, the weight is lost due to the evaporation of physically adsorbed water, and the weight lost is 1.3%; the second stage is from 220 °C to 680 °C with the weight loss value of 6.8%. The corresponding DTA curve has a strong absorption peak, indicating the removal of bound water from a portion of the hydrated mineral and the decomposition of carbonate and limestone to produce CO_2. When the temperature exceeds 700 °C, there is no significant change in the mass loss of the raw material, and the minimum firing temperature is 700 °C. On the basis of the TG analysis results, for complete reactions, 400 °C was selected as the pretreatment temperature; since the pore size of the sintered ceramic filter material increased with an increase in temperature, an excessive increase in temperature could cause the material to adhere.[29] Therefore, the sintering temperature chosen for this experiment was 1030 °C.

3.1.2 XRD. Fig. 2-1 shows the XRD patterns of the red mud powder before and after sintering. The results show that the raw red mud material contains quartz, gibbsite, and hematite. It can be seen that the minerals silicon, aluminum, and iron are the main components of red mud. Quartz is still the main phase in the spectrum of the sintered RMG, and the gibbsite peaks disappears after calcination because of its decomposition into aluminum oxide. The peak strength of hematite and alumina increases after sintering. The main reasons for this change were the transformation of other iron systems into hematite and the decomposition of gibbsite. Fig. 2-2 shows the XRD pattern of the SLRMG before and after the loading of Ca^{2+}, and it is not apparent from Fig. 2-2 that the absence of the characteristic peak of Ca^{2+} may be due to the insufficient loading or high dispersibility of Ca^{2+} on RMG.[27]

3.1.3 SEM. The morphology of the ceramic filter material was studied using SEM images. As shown in Fig. 3-a, the red mud powder has a smooth surface and a relatively smooth channel. The surface of the material is smooth, and the surface area is small. Fig. 3-b shows the image of the RMG filter material after sintering. At high temperatures, the sintered RMG exhibits the following characteristics: a fluffy appearance, more pore structures, and an increase in the number of folds in the pores; the porous structure and the discontinuous structure make the filter material attain the pore size of the particle surface, which provides a suitable condition for loading. Fig. 3-c

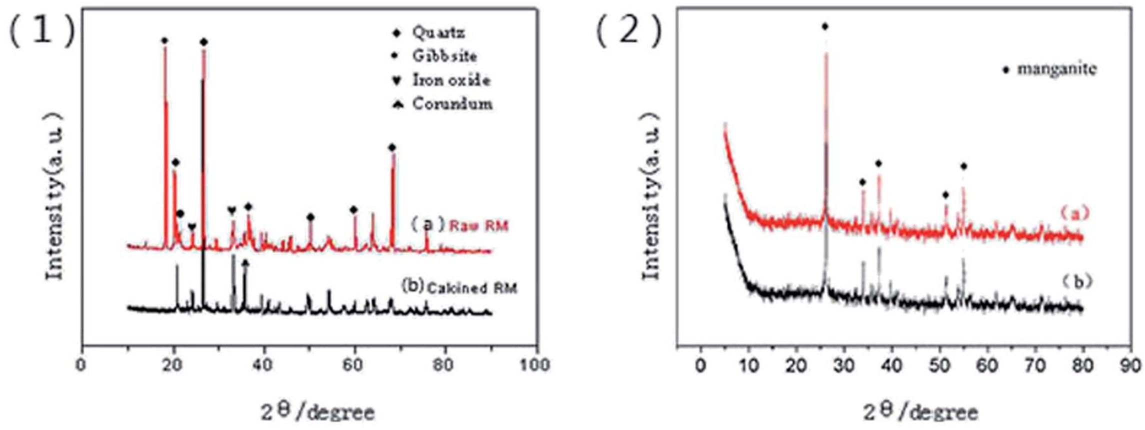

Fig. 2 XRD patterns of the (1-a) raw powder red mud, (1-b) calcined RMG material, (2-a) DLRMG and (2-b) SLRMG material.

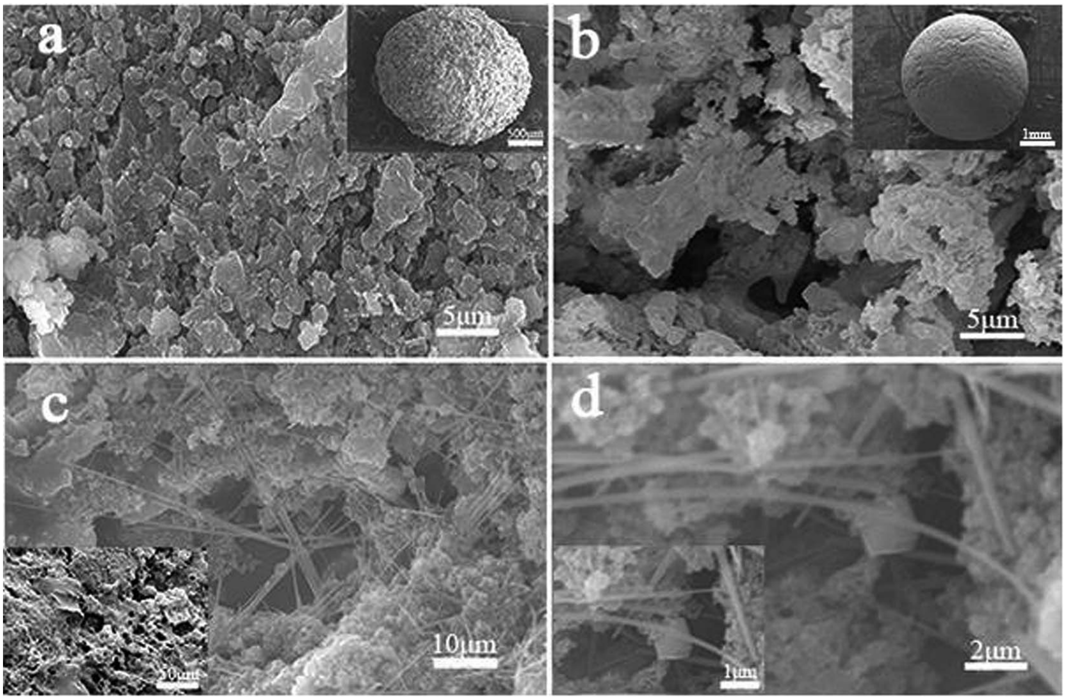

Fig. 3 SEM images of (a) raw RMG, (b) sintered RMG, (c) γ-MnOOH single loaded on RMG, and (d) Ca^{2+} loaded on γ-MnOOH/RMG.

shows that the shape of γ-MnOOH is nanorod. This demonstrates that the RMG particles loaded with γ-MnOOH on the surface and a large number of rod-shaped γ-MnOOH are arranged crosswise on the surface of the ceramic filter material and in the macropores.[30–32] Fig. 3-d shows a scanned image of γ-MnOOH/RMG loaded with Ca^{2+}. The results show that Ca^{2+} increases the specific surface area of the filter and enhances the adsorption capacity of the filter by entering the pore channel. The hardness, surface area and adsorption capacity of the red mud particles are improved after calcination. After loading Ca^{2+}

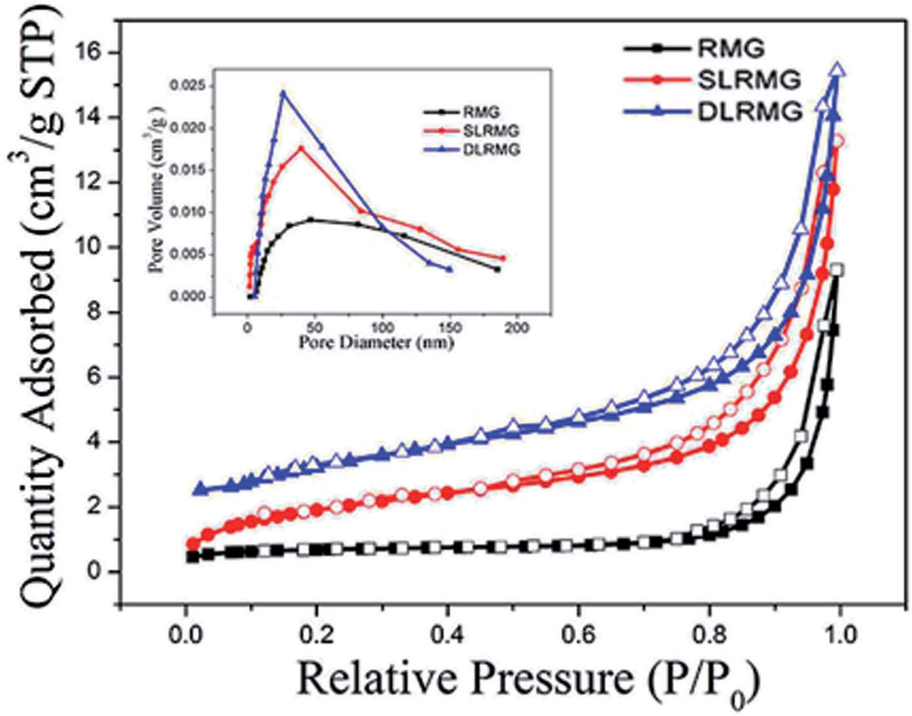

Fig. 4 Nitrogen adsorption–desorption isotherms and pore size distribution curves of RMG, SLRMG and DLRMG.

and γ-MnOOH, the surface area becomes larger; this is consistent with the BET result shown in Fig. 4.

3.1.4 BET analysis. Fig. 4 shows the nitrogen adsorption/desorption isotherms of RMG, SLRMG and DLRMG and the corresponding pore size distribution curves. Based on the IUPAC classification, the adsorption isotherms of the original filter media and the modified filter media samples show a typical IV adsorption behavior and an H3 hysteresis cycle. The typical characteristic is that the adsorption curve is inconsistent with the desorption curve. RMG shows a narrow hysteresis loop; however, the hysteresis loop of LRMG is much wider. The pore size distribution of the modified ceramic filter material has also changed. As observed in Fig. 4, RMG has only large mesopores and macropores with no obvious peak value; this indicates that the pore size distribution has dispersed; however, DLRMG has many mesopores and micropores that may be due to the uneven aggregation of small nanoparticles; the results are also in accordance with those obtained by SEM. Therefore, compared with the case of the original material, most of the modified pores are in the mesoporous range, and the supporting samples have many contact sites with reactants. The specific surface area of the modified material also confirms the possibility of high adsorption capacity of Fe^{2+} and Mn^{2+}. Table 2 presents the pore size, specific BET surface area and pore volume of the synthetic samples with different shapes. According to the data presented in Table 2, it is concluded that continuous modification of RMG increases the specific surface area and decreases the pore size.

3.1.5 Zeta potentials. The zeta potential of DLRMG and the saturated adsorptions of Fe^{2+} and Mn^{2+} by DLRMG were investigated at pH = 7. As shown in Fig. 5, the zeta potential decreased from 20.73 to −31.11 mV with an increase in pH from 1.0 to 9.0. The isoelectric point of RMG was 3.05 mV. As seen in Table 3, the zeta potential of DLRMG was −13.51 mV, which illustrated that the negatively charged surface of DLRMG would exert a positive effect on the removal of Fe^{2+} and Mn^{2+}. The zeta potentials of the supported samples decreased when compared with that of RMG at pH 7. Hence, the supported samples were more conducive to attract the positively charged ions. The zeta potential increased to −8.99 mV after adsorption.

3.2 Characteristics of the modified RMG in the Fe^{2+} and Mn^{2+} removal process

3.2.1 Effect of polyethylene glycol-400 addition on removal efficiency. The SLRMG samples were prepared using polyvinyl alcohol at different concentrations (additions were 3 mL, 2.5 mL, 2 mL, 1.5 mL, and 1 mL). Their Fe^{2+} and Mn^{2+} removal ability was compared at pH 7, as shown in Fig. 6. When the amount of polyethylene glycol-400 added was 2 mL, maximum removal rate of Fe^{2+} and Mn^{2+} was achieved, which was significantly higher than that of the pure RMG particles. This indicated that the presence of γ-MnOOH enhanced the ability of RMG particles to remove Fe^{2+} and Mn^{2+} when 2 mL of polyvinyl alcohol was added. The cross-distribution of the surface and the arrangement of the pores could be realized with the proper incorporation of γ-MnOOH. The adsorption efficiency increases with an increase in the number of adsorption sites. The reason for the adsorbance of Fe^{2+} being larger than that of Mn^{2+} was probably the small ion radius of Fe.[33] As the added amount of PEG-400 increased, the length of γ-MnOOH increased.

Table 2 Textural properties of RMG, SLRMG and DLRMG

Name	BET surface area ($m^2\ g^{-1}$)	Average pore width (nm)	Pore volume ($cm^3\ g^{-}$)
RMG	2.2529	26.2184	0.007
SLRMG	9.2422	12.4348	0.015
DLRMG	14.0702	9.6244	0.023

Table 3 Zeta potentials of RMG, DLRMG and after adsorption of Fe^{2+} and Mn^{2+} by DLRMG

	RMG	DLRMG	After adsorption
Zeta potentials	−10.97	−13.51	−8.99

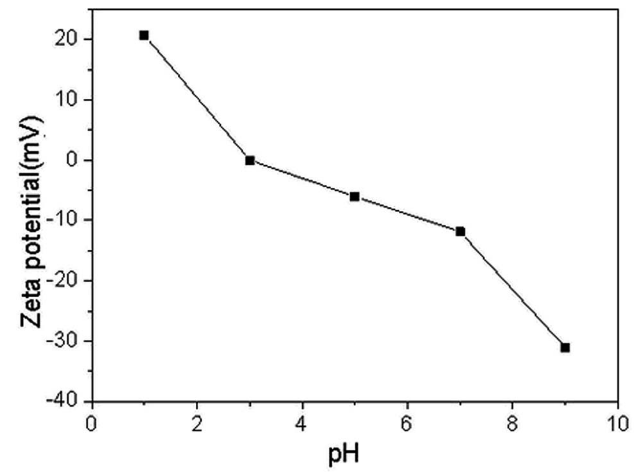

Fig. 5 Zeta potentials of RMG at different pHs.

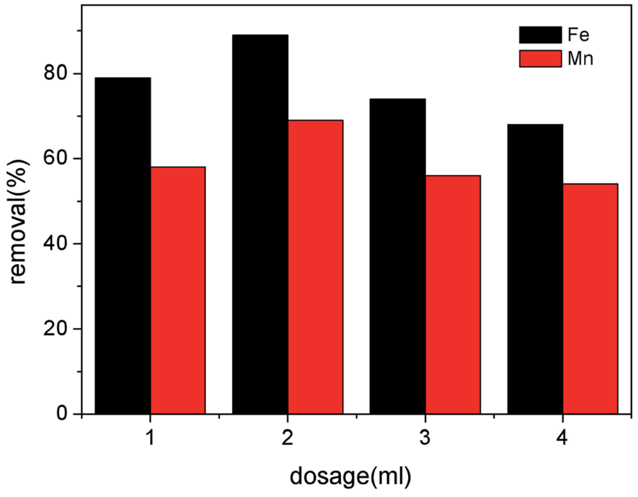

Fig. 6 Fe^{2+} and Mn^{2+} removal efficiencies by SLRMG at different additions of PEG-400.

Therefore, the effect of an additional amount of PEG-400 on the removal of Fe^{2+} and Mn^{2+} was taken into consideration during the preparation of an optimized adsorbent.

3.2.2 Effect of time, pH and dosage. With an increase in the reaction time, the removal rate of Fe^{2+} by RMG and DLRMG increased continuously and attained an adsorption equilibrium at 180 min. The supernatant concentration of RMG reached the Chinese drinking water standard at 3 h and that of DLRMG reached the Chinese drinking water standard at 2 h, and the removal rate of Fe^{2+} was up to 92.5 mg L^{-1}. With an increase in the reaction time, the removal rate of Mn^{2+} increased by the same process, and the removal rate of Mn^{2+} reached 90% when the reaction time was 2.5 h. The removal rate of Mn^{2+} by RMG and DLRMG increased continuously to reach an adsorption equilibrium at 180 min *via* the same procedure as that observed in the removal process of Fe^{2+}. As groundwater is mostly weakly alkaline, the set principle is based on the actual drinking water pH of 6–8. In this study, NaOH and HCl were used to regulate the pH. Based on the time of the maximum removal rate, the influence of different pH values on the removal rates of Fe^{2+} and Mn^{2+} was examined. As shown in Fig. 7b, the removal rate of Fe^{2+} increases with an increase in pH. The results showed that RMG-treated Fe^{2+} reached the effluent standard when pH > 7.5; on the other hand, DLRMG-treated Fe^{2+} reached the effluent standard at pH = 6.5; the trend of Mn^{2+} removal was equal to the tendency of Fe^{2+} removal. The removal rate of Mn^{2+} by RMG reached 90% at pH 7. DLRMG failed to meet the effluent Mn^{2+} content within the treatment range, and it achieved the effluent concentration at pH

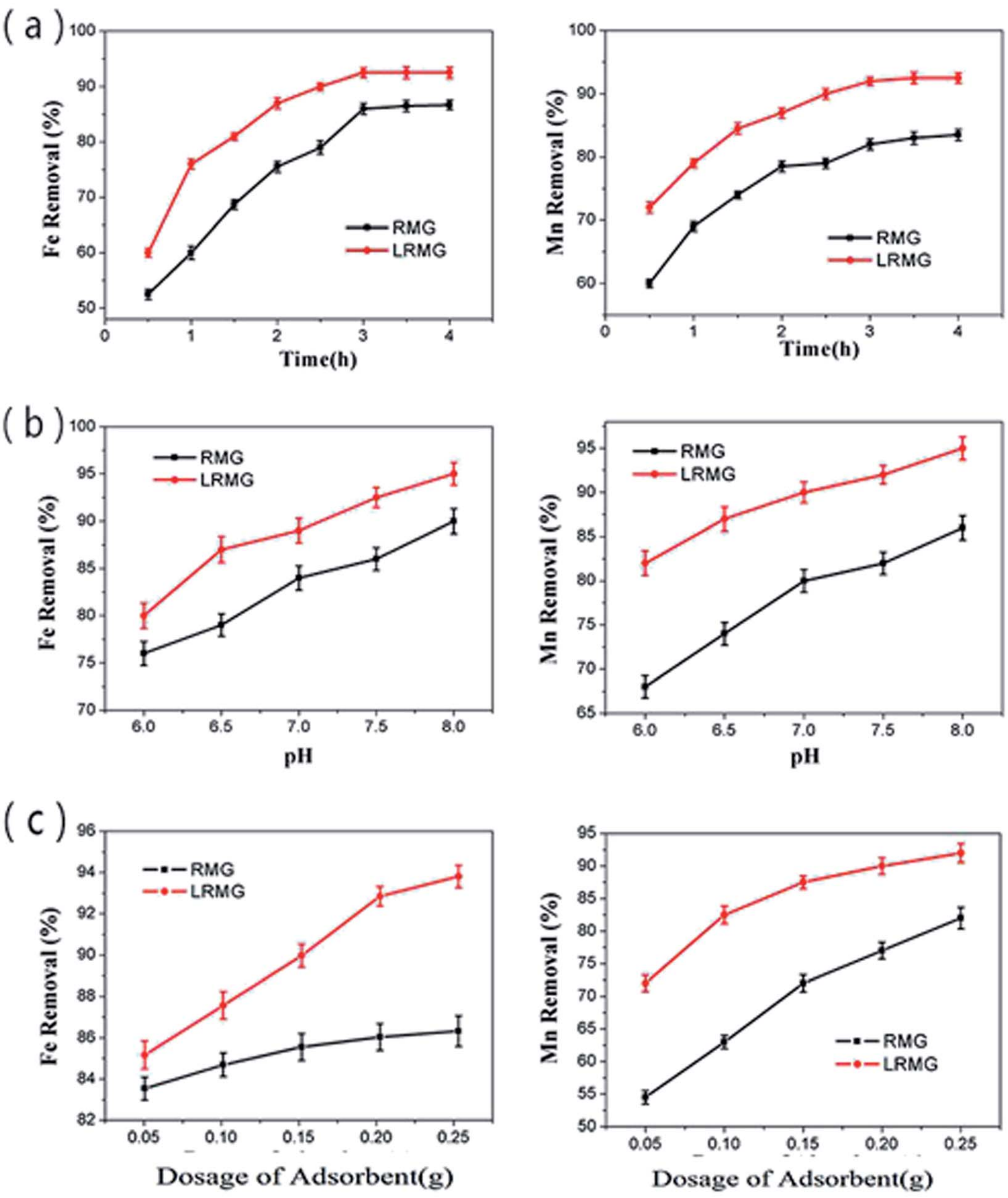

Fig. 7 (a) Fe^{2+} and Mn^{2+} removal efficiencies by RMG and DLRMG at different times; (b) Fe^{2+} and Mn^{2+} removal efficiencies by RMG and DLRMG at different pH values and (c) Fe^{2+} and Mn^{2+} removal efficiencies by RMG and DLRMG at different dosages of the adsorbent.

> 7. This showed that RMG was not enough to remove the manganese ions from water to achieve the standard during the process of Mn^{2+} removal, and the modified DLRMG could effectively remove Mn^{2+} under neutral pH conditions. In Fig. 7c, it is observed that the removal rate is proportional to the dosage. The removal rate of Fe^{2+} increased and reached an equilibrium with the continuous addition of RMG; when the addition amount of RMG was 0.25 g, there was no significant increase in the removal rate of Fe^{2+} when compared with the case of the dosage amount of 0.2 g; the tendency of adsorption efficiency with the continuous addition of DLRMG becomes slow after the addition of 0.2 g DLRMG. However, the effect of the dosage on Mn^{2+} removal was more significant when compared with that in the process of Fe^{2+} removal. When the dosage amount was 0.2 g, the removal rates for Fe^{2+} and Mn^{2+} were 93% and 90%, respectively. The effluent concentration reached the standard. Therefore, considering the preparation technology and the cost of the laboratory, we chose 0.2 g as the best dosage, thereby not only achieving the treatment effect but also using the resources effectively. DLRMG possessed the following characteristics: first, the removal pH was within the range of the groundwater pH. In most of the materials, the pH value needs to be adjusted in advance; however, it was unnecessary for DLRMG in this study. Second, the removal efficiency of the two pollutants was quite obvious, and there would not be a very uneven removal effect of the two pollutants. Both pollutants could be effectively removed by DLRMG. Finally, the removal of Fe^{2+} and Mn^{2+} by the proposed material was a simple process, which could be achieved by direct dosing.

3.3 Fe^{2+} and Mn^{2+} removal process and mechanism

3.3.1 Removal mechanism of the filter material. The preparation process of DLRMG is illustrated in Fig. 8. The arrangement of Ca^{2+}–γ-MnOOH on the surface of RMG showed that γ-MnOOH presented a one-dimensional hexahedral shape. Herein, the MnO_6 octahedral single chain shared the vertex and formed a 1 × 1 node tunnel containing protons.[34,35] Manganese contains more single-coordinated oxygen functional groups than goethite because of its comparative structure (*i.e.* single-chain and double-stranded split-edge octahedron). The Mn-based oxide nanomaterials with unsaturated valence have been used as excellent adsorbents.[36–39] The mechanism of removing Fe^{2+} and Mn^{2+} by the particle filter is illustrated in Fig. 8c. First, red mud had an electrostatic attraction to Fe^{2+} and Mn^{2+}. The isoelectric point of the sintered RMG material was 3.3. When $pH < 3.3$, the zeta potential of the sintered RMG material was positive. In contrast, the zeta potential of the sintered RMG material was negative when $pH > 3.3$, which would have a positive effect during the adsorption process of cation.[27] The zeta potential of RMG was −10.97 mV, indicating that RMG had a negative charge under the condition of $pH = 7$, which played an active role in the process of removing Fe^{2+} and Mn^{2+}. The surface potential obtained after loading showed negative when the pH value was weak alkali, which could increase the adsorption of cationic particles through electrostatic attraction. The zeta potential of DLRMG was −13.51 mV, which was more favorable to the adsorption of Fe^{2+} and Mn^{2+}. By successively loading γ-MnOOH and Ca^{2+}, the specific surface area of the filter media increased, such that more adsorption sites could be provided. Then, the zeta potential of red mud in water was negative because a large number of metal oxides were produced during the protonation of the surface hydroxyl group. The formation of the hydroxyl groups and supported γ-MnOOH on the surface of red mud could redox the pollutants in the water, thus oxidizing Fe^{2+} and Mn^{2+} to an insoluble and high valence state, which could be filtered and attached to the

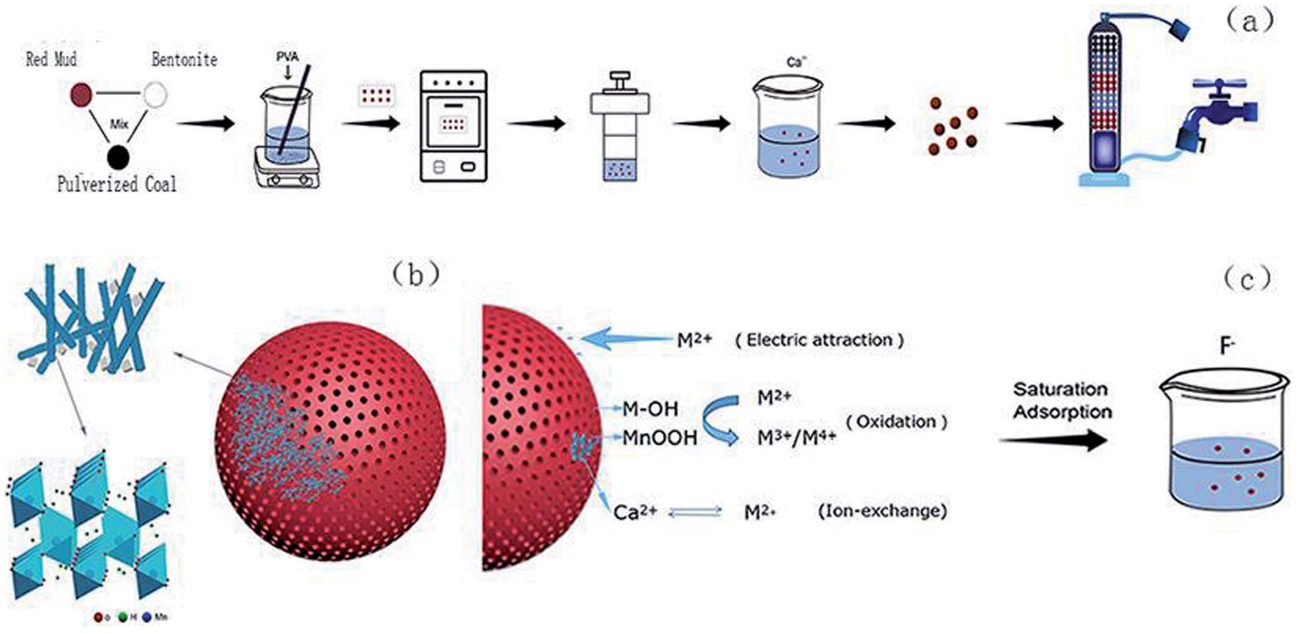

Fig. 8 (a) Preparation process of double-loaded RMG, (b) Ca^{2+}–γ-MnOOH on RMG, and (c) removal mechanism of Fe^{2+} and Mn^{2+} by RMG and subsequent treatment of fluorine-containing wastewater.

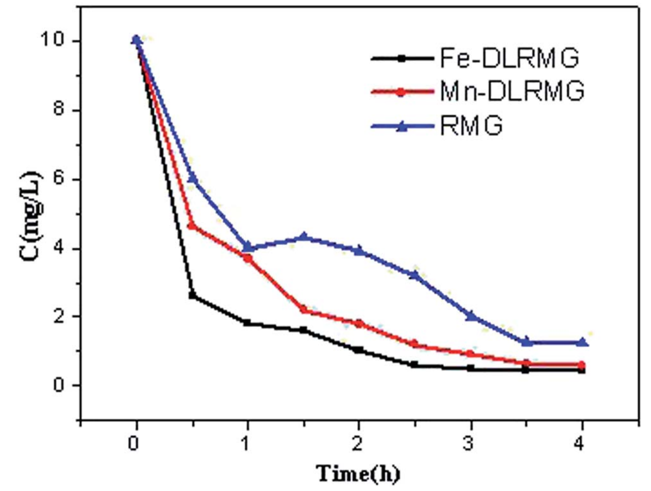

Fig. 9 Removal of F$^-$ by RMG, Fe-DLRMG and Mn-DLRMG.

surface of the granular filter media for removal. Finally, the adsorption of Fe^{2+} and Mn^{2+} by DLRMG was based on the ion exchange process. Ca^{2+} loaded on DLRMG can be able to proceed ion exchange reactions with Fe^{2+} and Mn^{2+} in water, which have been studied by M. E. kady *et al.*[40] and P. Chand *et al.*[41] Through the electric attraction, oxidation and ion exchange, Fe^{2+} and Mn^{2+} in water could be effectively adsorbed and removed.

3.4 Reuse of DLRMG

The reuse of adsorbents is very critical in practical applications. Traditional methods of elution using acid or alkali work well, but they are prone to additional contamination.[42] In this study, the DLRMG adsorbent that was saturated with Fe^{2+} and Mn^{2+} was proposed to be reused for continuous removal of excessive F$^-$. The two adsorbents RMG, and DLRMG after the adsorption of Fe^{2+} and Mn^{2+} were compared for the removal of F$^-$. As Fig. 9 showed that the removal rate is better which utilized after adsorption. By comparing the results of the adsorbed material with those of the reported literature,[43,44] it was found that the reused adsorbent had a good treatment effect and reached the standard after the treatment. The iron-adsorbed particles were stronger than the manganese-adsorbed particles because the amount of Fe^{2+} adsorbed on the particles was greater than that of Mn^{2+}. By comparing the effect of RMG, Fe-DLRMG, and Mn-DLRMG on the removal of F$^-$ in water (Fig. 9), we concluded that Fe-DLRMG was best for removal possibly due to the higher amount of Fe^{2+} on DLRMG.

4. Conclusion

Herein, a granular filter material was prepared with red mud as the carrier of Ca^{2+} and γ-MnOOH. The results showed that γ-MnOOH well dispersed in the macroporous structure of RMG, and Ca^{2+} added to the loaded granular filtration material further improved the removal capacity. Compared with RMG, DLRMG had higher surface area and uneven surface morphology and exhibited a better effect in Fe^{2+} and Mn^{2+} removal. The adsorbent obtained after the saturated adsorption of Fe^{2+} and Mn^{2+} was used to remove F$^-$ instead of the traditional elution process, and good removal efficiency was achieved. This shows that red mud is a promising material for heavy metal adsorption.

Conflicts of interest

There are no conflicts to declare.

Acknowledgements

This work was supported by a special fund project of Harbin Science and Technology Innovation Talents Research (2016RQQXJ109), Heilongjiang Provincial Institutions of Higher Learning Basic Research Funds Basic Research Projects (KJCX201812), Heilongjiang College Student Innovation and Entrepreneurship Training Program Project (201810212141), Harbin Jixin International Environmental Protection Creative Technology Training Project, and Natural Science Foundation of Heilongjiang Province (E201456).

References

1 F. A. Bertoni, J. C. González, S. I. García, L. F. Sala and S. E. Bellú, *Carbohydr. Polym.*, 2018, **180**, 55–62.
2 M. L. Lima, A. Romanelli and H. E. Massone, *Sci. Total Environ.*, 2015, **530–531**, 333–346.
3 Q. F. Cheng, L. C. Nengzi, L. L. Bao, Y. Huang, S. Y. Liu, X. W. Cheng, B. Li and J. Zhang, *Chemosphere*, 2017, **182**, 450–457.
4 C. Y. Li, S. T. Wang, X. P. Du, X. S. Cheng, M. Fu, N. Hou and D. P. Li, *Bioresour. Technol.*, 2016, **220**, 76–84.
5 S. Mirlohi, A. M. Dietrich and S. E. Duncan, *Environ. Sci. Technol.*, 2011, **45**, 6575–6583.
6 S. M. Rahman, M. Kippler, S. Ahmed, B. Palm, S. E. Arifeen and M. Vahter, *Reprod. Toxicol.*, 2015, **53**, 68–74.
7 Q. Tang, G. J. Liu, C. C. Zhou, H. Zhang and R. Y. Sun, *Chemosphere*, 2013, **93**, 2473–2479.
8 S. Y. Qina, F. Ma, P. Huang and J. X. Yang, *Desalination*, 2009, **245**, 183–193.
9 Y. H. Bai, Y. Y. Chang, J. S. Liang, C. Chen and J. H. Qu, *Water Res.*, 2016, **106**, 126–134.
10 S. L. D. Kenari and B. Barbeau, *Water Res.*, 2017, **113**, 50–61.
11 X. Du, G. Y. Liu, F. S. Qu, K. Li, S. L. Shao, G. B. Li and H. Liang, *Desalination*, 2017, **403**, 97–106.
12 A. G. Tekerlekopoulou, S. Pavloub and D. V. Vayenasa, *J. Chem. Technol. Biotechnol.*, 2013, **88**, 751–773.
13 D. Vries, C. Bertelkamp, F. S. Kegel, B. Hofs, J. Dusseldorp, J. H. Bruins, W. de Vet and B. van den Akker, *Water Res.*, 2017, **109**, 35–45.
14 K. S. Nitzsche, P. Weigold, T. Lösekann-Behrens, A. Kappler and S. Behrens, *Chemosphere*, 2015, **138**, 47–59.
15 D. I. Cifci and S. Meric, *Colloids Surf., A*, 2017, **522**, 279–286.
16 A. Ates and G. Akgül, *Powder Technol.*, 2016, **287**, 285–291.
17 C. Dalaia, R. Jhab and V. R. Desaic, *Aquatic Procedia*, 2016, **4**, 1126–1133.

18 Q. S. Si, Q. Zhu and Z. P. Xing, *ACS Sustainable Chem. Eng.*, 2017, **5**, 11422–11432.

19 Z. Guo, Q. Zhu, C. C. T. Liu and Z. P. Xing, *Constr. Build. Mater.*, 2018, **172**, 263–271.

20 I. B. Natályа, P. S. C. Santos, T. E. de Souza, L. C. A. Oliveira and C. S. Castro, *J. Hazard. Mater.*, 2016, **314**, 304–311.

21 N. Deihimi, M. Irannajad and B. Rezaim, *J. Environ. Manage.*, 2018, **206**, 266–275.

22 Y. Zhao, J. Wang, Z. K. Luan, X. j. Peng, Z. Liang and L. Shi, *J. Hazard. Mater.*, 2009, **165**, 1193–1199.

23 L. Li, Q. Zhu, K. X. Man and Z. P. Xing, *J. Mol. Liq.*, 2017, **237**, 164–172.

24 D. M. Han, M. J. Currell and G. L. Cao, *Environ. Pollut.*, 2016, **218**, 1222–1233.

25 B. Huang, Z. W. Li, Z. L. Chen, G. Q. Chen, C. Zhang, J. Q. Huang, X. D. Nie, W. P. Xiong and G. M. Zeng, *Environ. Sci. Pollut. Res.*, 2015, **22**, 19912–19921.

26 C. M. Kanno, R. L. Sanders, S. M. Flynn, G. Lessard and S. C. B. Myneni, *Environ. Sci. Technol.*, 2014, **48**, 5798–5807.

27 S. C. Chen, L. Fang, Q. Zhu, L. Li and Z. P. Xing, *RSC Adv.*, 2016, **6**, 28257–28262.

28 L. Y. Shao, Q. Zhao and J. Chen, *Chem. Commun.*, 2017, **23**, 2435–2438.

29 K. X. Man, Q. Zhu, L. Li, C. T. Liu and Z. P. Xing, *Ceram. Int.*, 2017, **43**, 7565–7572.

30 Z. C. Li, H. L. Bao, X. Y. Miao and X. H. Chen, *J. Colloid Interface Sci.*, 2011, **357**, 286–291.

31 M. Sun, B. Lan, T. Lin, G. Cheng, F. Ye, L. Yu, X. L. Cheng and X. Y. Zheng, *CrystEngComm*, 2013, **15**, 7010–7018.

32 L. L. Lan, G. R. Gu, Q. J. Li, H. F. Zhang, K. Xu, B. Liu and B. B. Liu, *RSC Adv.*, 2015, **5**, 25250–25257.

33 H. Yan, H. J. Li, X. Tao, K. Li, H. Yang, A. M. Li, S. J. Xiao and R. S. Cheng, *ACS Appl. Mater. Interfaces*, 2014, **6**, 9871–9880.

34 T. Hens, J. Brugger, S. A. Cumberland, B. Etschmann and A. J. Frierdich, *Environ. Sci. Technol.*, 2018, **52**, 1311–1319.

35 P. F. Smith, B. J. Deibert, S. Kaushik, G. Gardner, S. H. Wang, J. F. Al-Sharab, E. Garfunkel, L. Fabris, J. Li and G. C. Dismukes, *ACS Catal.*, 2016, **6**, 567–579.

36 S. Guo, W. Z. Sun, W. Y. Yang, Q. Li and J. K. Shang, *RSC Adv.*, 2015, **5**, 53280–53288.

37 S. Lan, H. Ying, X. M. Wang, F. Liu, W. F. Tan, Q. Y. Huang, J. Zhang and X. H. Feng, *Water Res.*, 2015, **128**, 92–101.

38 A. J. Frierdich, M. l J. Spicuzza and M. M. Scherer, *Environ. Sci. Technol.*, 2016, **50**, 6374–6380.

39 C. O. Dennis, S. M. B. Pingul-Ong, C. C. Kan and M. D. G. de Luna, *J. Cleaner Prod.*, 2018, **190**, 443–451.

40 M. E. kady, H. Shokryc and H. Hamad, *RSC Adv.*, 2016, **6**, 82244–82259.

41 P. Chand and Y. B. Pakade, *Environ. Sci. Pollut. Res.*, 2015, **22**, 10919–10929.

42 O. Krüger, U. Kalbe, W. Berger, K. Nordhauβ, G. Christoph and H.-P. Walzel, *Environ. Sci. Technol.*, 2012, **46**, 13085–13092.

43 V. Sivasankar, T. Ramachandramoorthy and A. Darchen, *Desalination*, 2011, **272**, 179–186.

44 K. Biswas, K. Gupta, A. Goswami and U. C. Ghosh, *Desalination*, 2010, **255**, 44–51.